The third term gives

$$\frac{p_3^2}{m^2c^2}=\frac{64u^2\mu^2}{9v^2b_{\min}^6}=\frac{4}{9}\,\alpha^2\left(\frac{m}{M_p}\right)^2\gamma^6\beta^4\;. \qquad \text{(A4)}$$

For $\gamma \lesssim 10$ these terms are small compared with unity and hence relativistic effects on the recoiling electron will not be large.

---

[*] World Health Organization Fellow. Present address: Health Physics Division, Oak Ridge National Laboratory, Oak Ridge, Tenn. 37830.

[1] H. A. Bethe, Ann. Physik 5, 325 (1930).

[2] H. A. Bethe, in *Handbuch der Physik*, edited by H. Geiger and Karl Scheel (Springer-Verlag, Berlin, 1933), Vol. 24/1, p. 491ff.

[3] N. Bohr, Phil. Mag. 25, 10 (1913).

[4] Leslie L. Foldy, Rev. Mod. Phys. 30, 471 (1958).

[5] U. Fano, Natl. Acad. Sci. Natl. Res. Council Publ. No. 1133, 1964 (unpublished).

[6] J. D. Jackson, *Electrodynamics* (Wiley, New York, 1962), p. 143.

[7] J. D. Jackson, in Ref. 6, pp. 380–381. The transformation appropriate to Fig. 1 is obtained from Jackson's Eq. (11.114) by interchanging the primed and unprimed symbols and reversing the sign in front of β. It is assumed that the origins of K and K' coincide at times $t=t'=0$.

[8] J. D. Jackson, in Ref. 6, p. 147.

[9] See, for example, E. Fermi, *Nuclear Physics* (Chicago U. P., Chicago, 1953).

[10] For the electron, of course, $\bar{u}=1$, but we write it in Eq. (21) explicitly to identify the physical origin of terms in Eq. (22).

[11] J. Baarli and A. H. Sullivan, Phys. Med. Biol. 14, 269 (1969).

[12] G. S. Hurst (private communication).

[13] L. G. Christophorou, R. N. Compton, G. S. Hurst, and P. W. Reinhardt, J. Chem. Phys. 43, 4273 (1965).

PHYSICAL REVIEW B VOLUME 3, NUMBER 9 1 MAY 1971

Electron-Paramagnetic-Resonance Investigation of the Dynamic Jahn-Teller Effect in $SrCl_2:La^{2+}$

J. R. Herrington[*] and T. L. Estle[*]
Physics Department, Rice University, Houston, Texas 77001
and
L. A. Boatner
Advanced Technology Center,[†] *Dallas, Texas* 75222

(Received 23 December 1970)

The electron-paramagnetic-resonance spectrum for $SrCl_2:La^{2+}$ has been observed between 1.2 and 40 °K. At 1.2 °K, the dominant structure is anisotropic and is described within experimental error by second-order solutions of the effective Hamiltonian for an isolated ^2E_g state split by large random internal strains. Coexisting with the anisotropic structure at temperatures between 1.2 °K and approximately 5 °K is structure whose position is isotropic but whose intensity and linewidth are anisotropic and vary with temperature and sample treatment. This structure is shown to result from rapid direct relaxation between the strain-split vibronic states. At temperatures above approximately 6 °K, only the isotropic structure is observed.

I. INTRODUCTION

The instability of a symmetric nonlinear polyatomic complex in an orbitally degenerate state was demonstrated theoretically by Jahn and Teller.[1] Early experimental evidence[2–4] indicated that the effects of this instability could be conveniently divided into two categories. Either the complex spontaneously became distorted and was stabilized in a configuration of lower symmetry (static Jahn-Teller effect), or the complex became distorted but, instead of being stabilized, was rapidly reoriented between several distorted configurations (dynamic Jahn-Teller effect). Anisotropic electron-paramagnetic-resonance (EPR) spectra characteristic of a static Jahn-Teller effect were first reported[2] for Cu^{2+} in trigonal sites of $ZnSiF_6\cdot 6H_2O$ at temperatures in the liquid-hydrogen range. Somewhat earlier, an isotropic EPR spectrum had been observed[3] at elevated temperatures for the same system and interpreted[4] as a thermally induced reorientation of the complex between equivalent static distortions, a type of dynamic Jahn-Teller effect. Subsequently, both types of spectra have been reported for a number of systems. These investigations and other studies of the Jahn-Teller effect have been reviewed by Sturge.[5]

Recently, anisotropic EPR spectra have been observed[6–11] which indicate the occurrence of another type of dynamic Jahn-Teller effect for orbital doublets at liquid-helium temperatures. The first such spectrum was reported by Coffman[6–8] for Cu^{2+} in MgO. Similar spectra were reported for Sc^{2+} in CaF_2 and SrF_2 by Höchli and Estle[9] and Höchli[10] and for Cu^{2+} in CaO by Coffman, Lyle, and Mattison.[11] Interpretations of these spectra were based on a strong vibronic-coupling model in which the dynamic character was attributed to tunneling between energetically equivalent static distortions. In each case an isotropic spectrum was observed to coexist with the anisotropic spectrum at intermediate temperatures (6–10 °K) and was attributed to thermal population of the excited "tunneling" singlet. This strong vibronic-coupling "tunneling" model had been developed earlier by Bersuker[12–14] and independently by O'Brien.[15]

An alternative explanation for the low-temperature dynamic effects for ^2E states based on moderate vibronic coupling has been given by Ham.[16,17] In this work, Ham has related the observable features of EPR spectra to the strength of the vibronic coupling. In so doing he demonstrated that certain parameters in the effective Hamiltonian were reduced from their values as predicted with a static crystal field model. The reduction factor q introduced by Ham[16,17] was shown to have a value between $\frac{1}{2}$ and 1 depending on whether the linear vibronic-coupling term was strong or weak. O'Brien[15] had previously shown that in the strong vibronic-coupling limit the reduction factor q could be slightly less than $\frac{1}{2}$ if nonlinear vibronic-coupling terms were considered. In addition, Ham[16,17] has shown that large random strains could cause the unique line shapes observed in the anisotropic spectra and that rapid relaxation between the strain-split vibronic states could average the anisotropic spectra yielding isotropic spectra.

Chase[18,19] recently proposed a test, independent of Ham's reduction factor, for the presence of a nearby excited "tunneling" singlet. He pointed out that coupling between the vibronic singlet and the vibronic doublet ground state (via the strain and Zeeman interactions in second order) would result in selective broadening of certain components in the observed line shape. This selective broadening would produce an anisotropic asymmetry in the line shape and could, in most cases, lead to an independent determination of the transformation properties of the tunneling singlet. As evidence for this hypothesis, Chase reported[18,19] the optically detected EPR from an excited ^2E state of Eu^{2+} in CaF_2 and SrF_2.

The preliminary EPR results for $SrCl_2:La^{2+}$, a $5d^1$ configuration impurity in eightfold coordination, presented earlier,[20,21] were consistent with Ham's moderate vibronic-coupling model. The present work reports additional observations for this system and a more complete analysis of the spectrum observed between 1.2 and 40 °K. The anisotropic spectrum is interpreted using Ham's effective Hamiltonian[16,17] and second-order perturbation solutions to this effective Hamiltonian account for the observed effects in the angular dependence. In addition, the isotropic spectrum will be discussed in greater detail than previously.[21]

This work represents the first complete analysis in terms of an effective Hamiltonian for a ^2E_g state of the EPR spectrum for an orbital doublet exhibiting a dynamic Jahn-Teller effect.

II. THEORY

A. Moderate Coupling Model

The EPR results reported here are found to be entirely consistent with the model illustrated in Fig. 1.

The La^{2+} impurity occupies a Sr^{2+} substitutional site in the $SrCl_2$ crystal (fluorite structure). The site symmetry is cubic (point group O_h) with eightfold coordination. The ground configuration of La^{2+} is $[Xe]5d^1$ and the free-ion ground term is a ^2D. The cubic crystal field splits the ^2D term as shown in Fig. 1 into ^2E_g or Γ_3^+ and $^2T_{2g}$ or Γ_5^+ levels with the ^2E_g level lowest. The cubic crystal field splitting Δ or $10Dq$ is on the order of 20 000 cm^{-1}. The ground vibronic multiplet resulting from moderate vibronic coupling is a ^2E_g vibronic state with the first-excited vibronic state roughly 140 cm^{-1} above the ground state.

As a result of random internal strains (10^{-4} to 10^{-5}), the ground vibronic doublet for each La^{2+} complex is split into two Kramers doublets with an average separation, δ in Fig. 1, of approximately 1 cm^{-1}. Due to a distribution in the magnitude of the strain, numerous pairs of Kramers doublets with varying separation are produced. For a given value of δ, the nature of each doublet depends on the ratio of those components of the strain which produce the splitting. In an EPR experiment, the spin degeneracy of each Kramers doublet is removed by the application of an external magnetic field and transitions (illustrated by arrows in Fig. 1) are stimulated between the spin states. The magnitude of the Zeeman splitting for each Kramers doublet

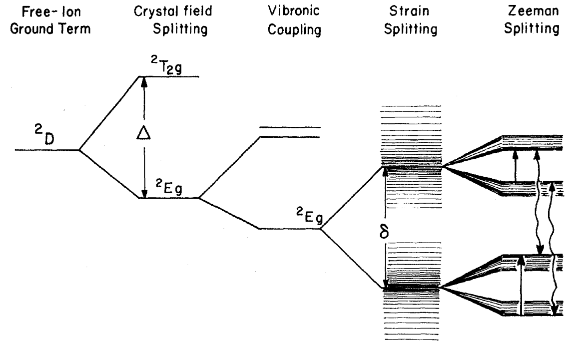

FIG. 1. Schematic energy-level diagram for the La^{2+} complex observed in $SrCl_2$.

depends on the strain-determined nature of the doublet. Hence the observed EPR line represents a superposition of many closely spaced transitions, its shape determined by the strain distribution.

Due to the large strain coupling (10^4 cm^{-1}), there exist relaxation transitions (represented by wavy arrows in Fig. 1) between the strain-split vibronic states in addition to the conventional spin-lattice relaxation processes. This vibronic relaxation proceeds by a direct process at low temperatures and is much more rapid than the spin-lattice relaxation. The rapid vibronic relaxation averages components of the anisotropic spectrum yielding an isotropic spectrum.

B. Effective Hamiltonian

The theory for the dynamic Jahn-Teller effect resulting from moderate vibronic coupling between an orbital doublet and a twofold-degenerate mode of vibration was developed by Ham.[16,17] In his treatment, Ham showed that the ground vibronic state was a doublet whose transformation properties were the same as the orbital doublet and that the first-excited vibronic state would be of the order of a few hundred cm^{-1} above the ground state. Thus, the ground state was treated as an isolated state and an effective Hamiltonian was formulated for this state.[16,17] The coupling parameters for the different terms in the effective Hamiltonian for the ground vibronic state were related by Ham[16,17] to the corresponding coupling parameters in the effective Hamiltonian for the orbital state determined using crystal field theory (zero vibronic coupling) by the reduction factors q and p.

Operators connecting the vibronic states within the ${}^2E_g$ ground manifold may be written in terms of four basic operators which transform like the components of the irreducible representations, $E_g \times E_g = A_{1g} + A_{2g} + E_g$. Only operators transforming like the irreducible representations contained in the direct product $E_g \times E_g$ may possess nonzero matrix elements connecting the vibronic states in the E_g manifold. Using as a basis vibronic wave functions which transform like $3z^2 - r^2$ and $\sqrt{3}\,(x^2 - y^2)$ (the θ and ϵ components of E_g, respectively), the four basic operators have the following matrix representation: (The upper right-hand matrix element in each operator corresponds to the $\langle\theta|\mathfrak{O}|\epsilon\rangle$ element.)

$$\mathfrak{A}_1 = \begin{pmatrix} 1 & 0 \\ 0 & 1 \end{pmatrix}, \quad \mathfrak{A}_2 = \begin{pmatrix} 0 & -i \\ i & 0 \end{pmatrix},$$

$$\mathcal{E}_\theta = \begin{pmatrix} -1 & 0 \\ 0 & 1 \end{pmatrix}, \quad \mathcal{E}_\epsilon = \begin{pmatrix} 0 & 1 \\ 1 & 0 \end{pmatrix}, \tag{1}$$

where $\mathfrak{A}_1$, $\mathfrak{A}_2$, $\mathcal{E}_\theta$, and $\mathcal{E}_\epsilon$ are vibronic operators transforming, respectively, like the A_{1g} and A_{2g} and the θ and ϵ components of the E_g irreducible representations of the point group O_h. An effective Hamiltonian for the ${}^2E_g$ manifold consists of invariant linear combinations of products of spin operators, vibronic operators, and components of fields.

An effective Hamiltonian representing the strain and Zeeman interactions is

$$\mathcal{H} = qV_s(e_\theta \mathcal{E}_\theta + e_\epsilon \mathcal{E}_\epsilon) + g_1 \mu_B \vec{\mathrm{H}} \cdot \vec{\mathrm{S}} \mathfrak{A}_1 + \tfrac{1}{2} q g_2 \mu_B [(3H_z S_z - \vec{\mathrm{H}} \cdot \vec{\mathrm{S}}) \mathcal{E}_\theta + \sqrt{3}\,(H_x S_x - H_y S_y) \mathcal{E}_\epsilon], \tag{2}$$

where $2e_\theta = 2e_{zz} - e_{xx} - e_{yy}$ and $2e_\epsilon = \sqrt{3}(e_{xx} - e_{yy})$ are those components of the strain transforming like $3z^2 - r^2$ and $\sqrt{3}\,(x^2 - y^2)$; H_x, H_y, and H_z are components of the magnetic field with respect to the cubic axes; S_x, S_y, and S_z are standard spin operators; and qV_s, $g_1\mu_B$, and $\frac{1}{2}qg_2\mu_B$ are coefficients representing the strength of the individual interactions. The reduction factor q is included explicitly so that one can use the expressions for V_s, g_1, and g_2 derived for the ${}^2E_g$ orbital state using static crystal field theory.

Assuming that the strain interaction determines the composition of the vibronic states, one obtains the following solution (see Appendix A):

$$E_{\pm, m_S} = \pm qV_s(e_\theta^2 + e_\epsilon^2)^{1/2} + g_1 \mu_B H m_S \left[1 \pm \left(\frac{qg_2}{g_1}\right) f_1 + \left(\frac{qg_2}{g_1}\right)^2 f_2\right]^{1/2}, \tag{3}$$

where ± refer to the two Kramers doublets. The functions f_1 and f_2 are defined in the following manner:

$$\begin{aligned} f_1 &= (3n^2 - 1)\cos\varphi + \sqrt{3}\,(l^2 - m^2)\sin\varphi, \\ f_2 &= \tfrac{1}{2} + \tfrac{1}{4}(3n^2 - 1)\cos 2\varphi - \tfrac{1}{4}\sqrt{3}\,(l^2 - m^2)\sin 2\varphi, \end{aligned} \tag{4}$$

the angle φ is determined by the ratio of e_ϵ to e_θ, i.e.,

$$\tan\varphi = e_\epsilon / e_\theta, \tag{5}$$

and l, m, and n are the direction cosines of the magnetic field with respect to the cubic axes. The EPR transitions occur at

$$H_\pm = \frac{h\nu}{g_1 \mu_B} \left[1 \pm \left(\frac{qg_2}{g_1}\right) f_1 + \left(\frac{qg_2}{g_1}\right)^2 f_2\right]^{-1/2}. \tag{6}$$

From Eqs. (4)–(6), it is apparent that the position of the EPR lines depends not on the magnitude of the strain at the site but merely on the distribution of the strain between the e_θ and e_ϵ components, i.e., upon φ. Ham[16,17] has shown that if one assumes that each EPR line is a δ function and that every value of φ is equally probable, then one obtains the strain envelope, correct to first order in qg_2/g_1, illustrated in Fig. 2(a). This may be seen by expanding Eq. (6) to obtain the first-order solution given by Eq. (7):

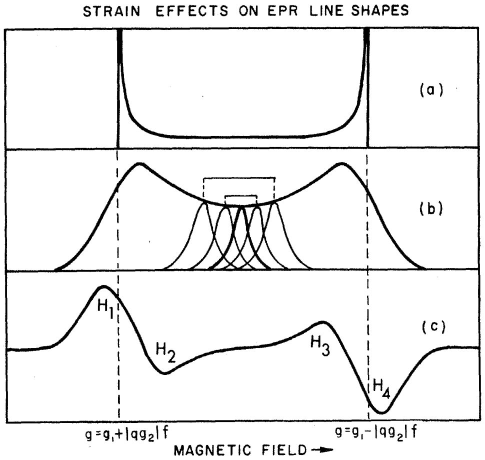

FIG. 2. EPR line shapes predicted in first order by Eq. (7) assuming all values of φ [defined in Eq. (5)] occur with equal probability: (a) each transition in the envelope is assumed to be a δ function of magnetic field; (b) each transition in the envelope is a Gaussian function of magnetic field with a linewidth equal to $\frac{1}{10}$ of the separation between the extrema; and (c) a first-derivative presentation of the envelope in (b).

$$H_\pm = \frac{h\nu}{g_1\mu_B}\left[1 \mp \frac{1}{2}\left(\frac{qg_2}{g_1}\right)f_1\right]$$

$$= \frac{h\nu}{g_1\mu_B}\left[1 \mp \left(\frac{qg_2}{g_1}\right) f\cos(\varphi-\alpha)\right] . \qquad (7)$$

In Eq. (7), f, φ, and α are defined in the following manner:

$$\tan\varphi = \frac{e_\epsilon}{e_\theta} , \quad \tan\alpha = \frac{\sqrt{3}\,(l^2-m^2)}{(3n^2-1)} ,$$
$$f = [1 - 3(l^2m^2 + m^2n^2 + n^2l^2)]^{1/2} . \qquad (8)$$

The extrema of the strain envelope are located at the same position as the two EPR lines predicted by a zero-strain solution [i.e., $\cos(\varphi-\alpha) = \pm 1$]. The effect of large internal strain on the observed EPR spectrum is to distribute the EPR lines between the two extrema of the strain envelope. How these lines are distributed is determined by the distribution in φ, which normally is uniform but which in any event is determined by how the strain is distributed between the e_θ and e_ϵ components.

The effects of the inherent width of each EPR line on the shape of the first-order strain envelope were evaluated numerically and typical results are shown in Figs. 2(b) and 2(c). It is apparent from Fig. 2(c) that the location of the extrema of the strain envelope are not simply related to the zero crossings in a first derivative presentation. The following procedure was formulated in which the location of the extrema were related to the position of the four features of the strain envelope labeled by H_1, H_2, H_3, and H_4 in Fig. 2(c): (a) determine $|H_1 - H_2|$ and $|H_3 - H_4|$; (b) the low-field extremum was located at $H_1 + \frac{1}{5}|H_1 - H_2|$; (c) the high-field extremum was located at $H_4 - \frac{1}{5}|H_3 - H_4|$. This procedure properly located the extrema of the strain envelope, insensitive to the assumed width or assumed shape (Lorentzian or Gaussian or a mixture of both) of the EPR lines comprising the strain envelope.

Combining Eq. (2) with an effective Hamiltonian for the hyperfine interaction one obtains

$$\mathcal{H} = qV_s(e_\theta\mathcal{E}_\theta + e_\epsilon\mathcal{E}_\epsilon) + g_1\mu_B\vec{H}\cdot\vec{S}\mathcal{A}_1$$
$$+ \tfrac{1}{2}qg_2\mu_B[(3H_zS_z - \vec{H}\cdot\vec{S})\mathcal{E}_\theta$$
$$+ \sqrt{3}\,(H_xS_x - H_yS_y)\mathcal{E}_\epsilon] + A_1\vec{I}\cdot\vec{S}\mathcal{A}_1$$
$$+ \tfrac{1}{2}qA_2[(3I_zS_z - \vec{I}\cdot\vec{S})\mathcal{E}_\theta + \sqrt{3}\,(I_xS_x - I_yS_y)\mathcal{E}_\epsilon] , \qquad (9)$$

where $\mathcal{A}_1$, $\mathcal{E}_\theta$, and $\mathcal{E}_\epsilon$ are the vibronic operators defined in Eq. (1); $\vec{H}$, $\vec{S}$, and $\vec{I}$ are, respectively, the magnetic field, the electronic-spin angular momentum, and the nuclear-spin angular momentum. The coefficients qV_s, $g_1\mu_B$, $\frac{1}{2}qg_2\mu_B$, A_1, and $\frac{1}{2}qA_2$ represent the strength of the different interactions with the reduction factor included explicitly, so that $g_1\mu_B$, $\frac{1}{2}g_2\mu_B$, A_1, and $\frac{1}{2}A_2$ would correspond to the coupling parameters for the ^2E_g orbital state derived using crystal field theory. By transforming this Hamiltonian to a new coordinate system (x', y', z') such that the z' axis is parallel to the applied magnetic field and assuming that qg_2/g_1, qA_2/A_1, and $A_1/g_1\mu_BH$ are small, the following solution is obtained, correct to second order, assuming that the strain interaction determines the composition of the vibronic states (see Appendix B):

$$H_{\pm,m_I} = \frac{h\nu}{g_\pm\mu_B} - \frac{A_1}{g_\pm\mu_B}\left[1 \pm \frac{1}{2}\frac{qA_2}{A_1}f_1 + \left(\frac{qA_2}{A_1}\right)^2 f_3 + 2\left(\frac{qg_2}{g_1}\right)\left(\frac{qA_2}{A_1}\right)f_3\right]m_I - \frac{(qA_2)^2}{h\nu g_\pm\mu_B}f_3m_I^2$$
$$-\left(\frac{(A_1 \mp \frac{1}{4}qA_2f_1)^2}{2h\nu g_\pm\mu_B} + \frac{(qA_2)^2}{h\nu g_\pm\mu_B}f_4\right)[I(I+1) - m_I^2] \qquad (10)$$

The functions $q_\pm$, f_1, f_3, and f_4 are defined by

$$g_\pm = g_1\left[1 \pm \frac{1}{2}\left(\frac{qg_2}{g_1}\right)f_1 + \left(\frac{qg_2}{g_1}\right)^2 f_3\right] , \qquad f_1 = (3n^2-1)\cos\varphi + \sqrt{3}\,(l^2-m^2)\sin\varphi ,$$

$$f_3 = \frac{9(l^2+m^2)n^2}{8}\cos^2\varphi - \frac{3\sqrt{3}\,(l^2-m^2)n^2}{8}\sin 2\varphi + \frac{12l^2m^2+3n^2(1+n^2)-6n^4}{8}\sin^2\varphi \ , \tag{11}$$

$$f_4 = \frac{9(l^2+m^2)^2}{32}\cos^2\varphi + \frac{3\sqrt{3}\,(l^2-m^2)(1+n^2)}{32}\sin 2\varphi + \frac{3[(l^2-m^2)^2+4n^2]}{32}\sin^2\varphi \ .$$

From Eq. (10) it can be seen that the hyperfine interaction produces $2I+1$ strain envelopes, each of which is similar to the strain envelope discussed previously for the strain and Zeeman interaction and illustrated in Fig. 2.

III. EXPERIMENT

A. Sample Preparation

The single crystals of $SrCl_2$ doped with La employed in this investigation were grown from the melt by a vertical Bridgman technique. The $SrCl_2$ powder was dried by heating under vacuum for 5 days at approximately 500 °C. Carefully dried $SrCl_2$ and $LaCl_3$ powders were sealed in an evacuated quartz ampoule which was then lowered at a rate of 2 cm per day through a Bridgman furnace operating at a maximum temperature of 925 °C. Single-crystal growth was facilitated by the presence of a sharp temperature gradient established by a cylindrical copper insert. The crystals of $SrCl_2$:La produced by this technique were optically clear but exhibited a strong blue fluorescence when exposed to near-ultraviolet radiation ($\lambda = 3660$ Å).

EPR was not detected in the "as-grown" $SrCl_2$:La crystals, indicating that the La impurity entered the $SrCl_2$ lattice predominantly in the trivalent state, La^{3+} ([Xe] configuration). The first method chosen to produce the desired divalent charge state was heating in strontium vapor. This selection proved fortunate for the investigation of the effects of random internal strains and vibronic relaxation phenomena.

The La^{3+} was reduced by loading $SrCl_2$:La crystals and Sr cuttings into quartz ampoules in a dry-nitrogen atmosphere. The ampoules were then evacuated, sealed, and inserted into a furnace operating at a temperature of 590 °C, removed after times varying from 5 to 45 min, and quenched in glycerine. The appearance of the crystals was altered by this reduction procedure from optically clear to opaque with a bright black metallic sheen. Strong EPR signals were observed. Heating at higher temperatures or for longer times resulted in samples which fractured easily, indicating the presence of very large internal strains. These severely strained samples exhibited either very weak or no observable EPR.

The stability of the charge state produced by this vapor-reduction technique was demonstrated by annealing reduced crystals at 200 °C for 6 h with no apparent decrease in the strength of the EPR signal. Subsequently, reduction has been accomplished using γ rays from a high-flux ^{137}Cs source. After γ irradiation at room temperature with a dose of 7×10^6 rad, the crystal changed from optically clear to a dark blue color. The observed EPR spectrum was identical with that obtained from vapor-reduced samples. The La^{2+} charge state produced by γ irradiation decayed rapidly at room temperature but could be stabilized at 77 °K.

B. Procedure

The EPR spectrum was observed using a reflection-homodyne spectrometer operating at a frequency of 8.9 GHz. The observed transitions did not saturate easily, hence the spectrometer was operated with approximately 1 mW of power incident on the cavity for optimum performance.

The samples were mounted in a TE_{102}-mode rectangular cavity utilizing the intersection of two $\{111\}$ cleavage planes to align a $\langle 110\rangle$ axis perpendicular to the plane of rotation of the applied magnetic field. This orientation permitted observations of the EPR spectrum along each of the three principal crystallographic directions by simply rotating the applied magnetic field. Precision alignment was achieved by an independent rotation of the crystal in a plane perpendicular to the plane of rotation of the applied magnetic field.

IV. EXPERIMENTAL RESULTS AND ANALYSIS

A. Anisotropic Spectrum

The EPR spectrum observed at 1.2 °K for a $SrCl_2$:La sample reduced in Sr vapor for 5 min is shown in Fig. 3 for the three high-symmetry directions, $\langle 100\rangle$, $\langle 111\rangle$, and $\langle 110\rangle$. The spectrum observed at each orientation was composed of eight components, each with a line shape resembling that of the strain envelope illustrated in Fig. 2(c). The extrema for each of the eight components are plotted on a horizontal scale below each trace; the upper bars locate the low-field set of extrema and the lower bars locate the high-field set of extrema. The dashed vertical lines locate the positions of the eight components observed for the $\langle 111\rangle$ orientation.

For the applied magnetic field oriented parallel to a $\langle 100\rangle$ crystallographic direction, the difference in magnetic field position between the two extrema for each of the eight components was a maximum, as seen in Fig. 3(a). For the applied field parallel to a ⟨111⟩ direction, Fig. 3(b), a more conventional line shape is observed as the two extrema for each component coincide. Figure 3(c) shows the spectrum observed for a ⟨110⟩ orientation of the applied field.

The positions of the extrema of each component of the spectrum were observed to agree with the predictions of Eqs. (10) and (11) for $I=\frac{7}{2}$ (the nuclear spin for the 99.91% naturally abundant ^{139}La isotope is $\frac{7}{2}$) and $\cos\varphi=\pm 1$. This comparison was complicated by the problem of locating the actual extrema of each component. Using the procedure outlined in Sec. II B, the locations of the extrema were determined as a function of the orientation of the applied field in a {110} plane and are shown in Fig. 4 by the open circles. The angular dependence in Fig. 4 is dominated by the first-order terms in Eqs. (10) and (11) but the observation that the average of the position of the extrema for each component at any orientation does not lie on a horizontal line drawn through the position of the corresponding component at the ⟨111⟩ orientation in Fig. 4 indicates that second-order terms must also be included.

The effective Hamiltonian parameters listed in Table I were obtained by a least-squares fit of the positions of the extrema for the ⟨100⟩ spectrum to the following expression which results from Eqs. (10) and (11) particularized for $\vec{H} \parallel \langle 100\rangle$ ($l=m=0$; $n=1$) and $\varphi=0$:

$$H_{\pm,m_I}=\frac{h\nu}{(g_1\pm qg_2)\mu_B}-\frac{A_1\pm qA_2}{(g_1\pm qg_2)\mu_B}\,m_I-\frac{(A_1\mp\frac{1}{2}qA_2)^2}{2h\nu(g_1\pm qg_2)\mu_B}\left(\tfrac{63}{4}-m_I^2\right). \tag{12}$$

The algebric sign of one parameter is determined in terms of the signs of the other three parameters. Using the parameters determined in this manner, the angular dependence of the extrema was calculated using Eqs. (10) and (11) and is shown by the solid curves in Fig. 4. This agreement is within experimental uncertainty but a first-order analysis was not.

TABLE I. Effective Hamiltonian parameters for $SrCl_2:La^{2+}$.

Parameter	Value	Accuracy
g_1	1.8808	±0.0005
qg_2	−0.0687	±0.0005
$A_1(10^{-4}\,cm^{-1})$	−119.5	±0.25
$qA_2(10^{-4}\,cm^{-1})$	−18.8	±0.25
q	0.57	±0.02

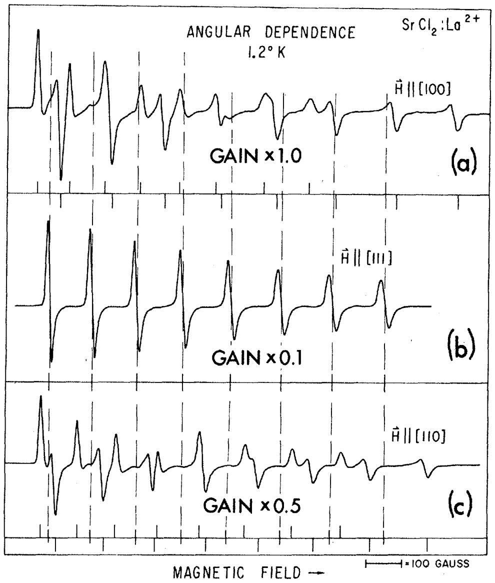

FIG. 3. EPR spectrum observed (ν = 8.9 GHz) at 1.2 °K for a $SrCl_2$: La sample reduced with Sr vapor for 5 min. The first derivative of absorption is shown versus magnetic field for the three high-symmetry directions: (a) $\vec{H} \parallel \langle 100\rangle$, (b) $\vec{H} \parallel \langle 111\rangle$, and (c) $\vec{H} \parallel \langle 110\rangle$. The extrema of the components of the spectrum are located by vertical bars on a horizontal scale below each trace. The dashed vertical lines locate the position of each of the eight components observed for $\vec{H} \parallel \langle 111\rangle$.

Upon careful examination of the spectra in Fig. 3, two additional qualitative features were noted: (a) The eight components in the ⟨111⟩ spectrum apparently did not have the same linewidth, and (b) the positive peak in the first-derivative presentation of absorption vs magnetic field located near the low-field extremum appeared more intense than the negative peak near the high-field extremum for the same component.

Equations (10) and (11) predict that with the field aligned along a ⟨111⟩ direction, the extrema for each component of the spectrum should exactly coincide and hence the spectrum should consist of eight lines of equal intensity and with equal linewidths. This was not observed even though the crystal was carefully aligned using two orthogonal rotations. The differences in linewidths are believed due to mosaic structure, i.e., the ⟨111⟩ direction for one La^{2+} site differs slightly from that of another La^{2+} site.

We have found that second-order effects of the Zeeman interaction can cause an asymmetry in the strain envelope shown in Fig. 2(c), i.e., the positive peak near the low-field extremum would be sharper than the negative peak near the high-field extremum in a first-derivation presentation. This asymmetry differs from that reported by Chase[18,19] in that the positive peak near the low-field extremum is always sharper than the negative peak. This predicted asymmetry is consistent with such data

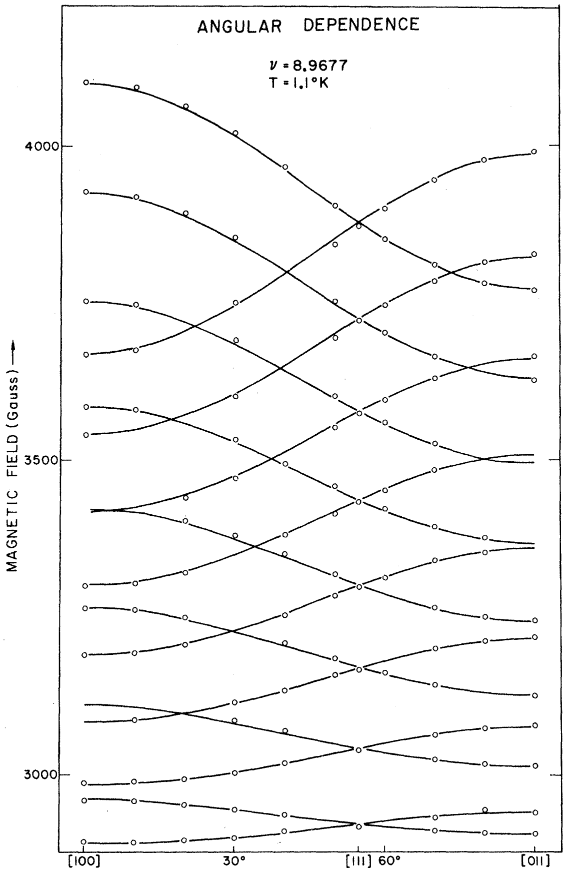

FIG. 4. Angular dependence of the extrema of each component of the anisotropic pattern observed for $SrCl_2:La^{2+}$ at 1.2 °K is shown as a function of the applied magnetic field oriented in a {110} plane. The open circles denote the measured positions of extrema. The solid lines were predicted by Eqs. (10) and (11) using the parameters listed in Table I.

as those in Figs. 3(a) and 3(c).

B. Isotropic Spectrum

In samples reduced in Sr vapor for times longer than 5 min, an isotropic eight-line pattern which coexisted with the anisotropic pattern previously discussed was observed at temperatures as low as 1.2 °K. The temperature dependence of the pattern for a sample reduced for 30 min is shown in Figs. 5 and 6 for the ⟨100⟩ and the ⟨110⟩ orientations, respectively. The extrema of the anisotropic pattern are located by the vertical bars on the horizontal scale at the bottom of the figure and the transitions in the isotropic pattern are located by the dashed vertical lines. Each of the transitions in the isotropic pattern is located approximately halfway between the two extrema of the corresponding anisotropic component. It is apparent that the positions of these lines are approximately the same as the eight components of the ⟨111⟩ anisotropic spectrum in Fig. 3(b). The spectra observed at 6 °K for a ⟨110⟩ and a ⟨111⟩ orientation of the applied magnetic field are shown in Fig. 7. In Fig. 8, the ⟨110⟩ spectrum observed at 4.2 °K for samples reduced with Sr vapor for 30 min, 15 min, and 5 min, respectively, are shown. (In Ref. 21, Fig. 3 was incorrectly labeled a ⟨100⟩ orientation, whereas it was actually ⟨110⟩.) Again the extrema of the anisotropic pattern are located by vertical bars on a scale at the bottom of the figure and the isotropic lines are located by the dashed vertical lines. The following characteristics of the isotropic pattern were noted: (a) the apparent intensity (peak-to-peak amplitude in first-derivative presentation) of each component of the isotropic pattern increases approximately linearly with temperature between 1.2 and 4.2 °K, Figs. 5 and 6; (b) the positive and negative peaks of the anisotropic pattern located near the extrema appear to broaden with increasing temperature, Figs. 5 and 6; (c) the apparent intensities of the isotropic lines decrease with increasing field, Figs. 5–7; (d) the apparent intensities of the isotropic lines increase as the field approaches a ⟨111⟩ orientation, Figs. 5–7; (e) the apparent intensity of the components of the isotropic pattern increases with increasing time of reduction with Sr vapor, Fig. 8; (f) the peaks in the anisotropic pattern broaden with increasing time of reduction with Sr vapor.

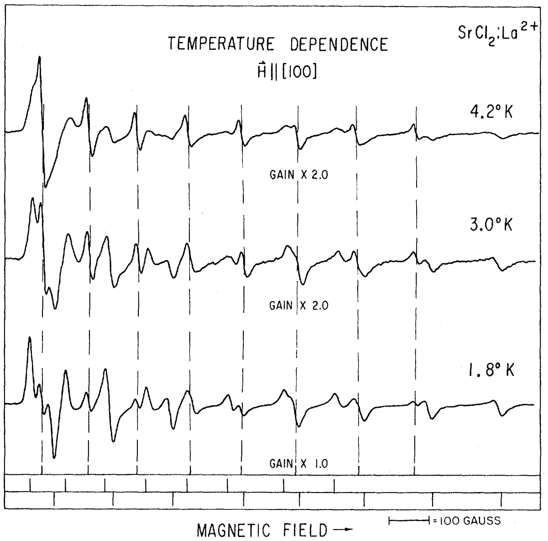

FIG. 5. Temperature dependence of the EPR spectrum observed ($\nu = 8.9$ GHz) for a ⟨100⟩ orientation of the applied field for a $SrCl_2:La$ sample reduced 30 min with Sr vapor at $T = 4.2$ °K, $T = 3.0$ °K, and $T = 1.8$ °K. The first derivative of absorption is shown versus magnetic field. The extrema of the anisotropic pattern are located by vertical bars on a horizontal scale at the bottom of the figure. The dashed vertical lines locate the positions of the eight isotropic lines.

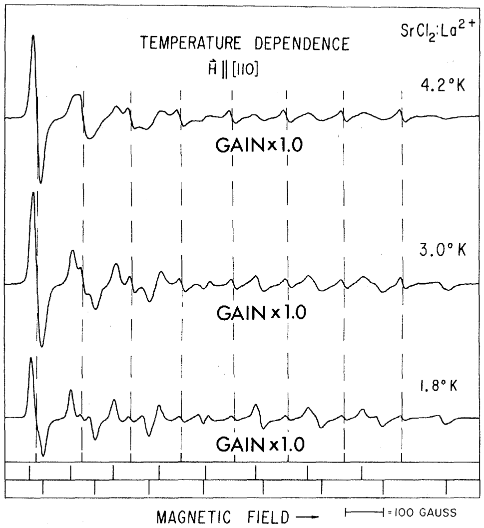

FIG. 6. Temperature dependence of the EPR spectrum observed ($\nu = 8.9$ GHz) for a $\langle 110 \rangle$ orientation of the applied field for a $SrCl_2$:La sample reduced for 30 min with Sr vapor at $T = 4.2$ °K, $T = 3.0$ °K, and $T = 1.8$ °K. The first derivative of absorption is shown versus magnetic field. The extrema of the anisotropic pattern are located by vertical bars on a horizontal scale at the bottom of the figure. The dashed vertical lines locate the positions of the eight isotropic lines.

Two explanations for this isotropic pattern have been advanced: (i) the isotropic pattern is due to transitions within an excited vibronic state,[6–11,18,19] and (ii) the isotropic pattern is due to averaging of a portion of the anisotropic spectrum caused by rapid relaxation between the strain-split components of the ground vibronic state.[16,17,20,21]

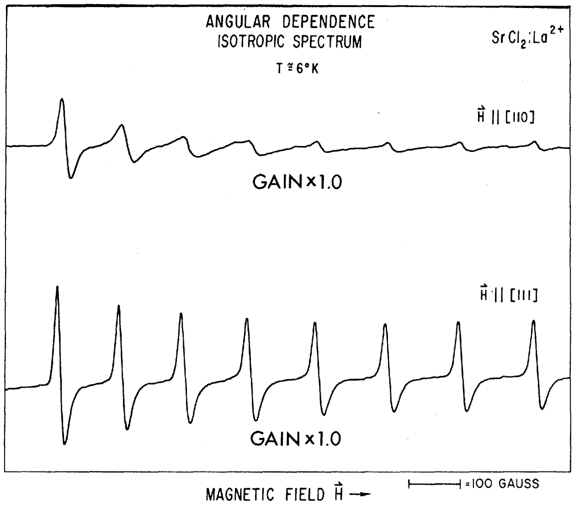

FIG. 7. EPR spectrum observed ($\nu = 8.9$ GHz) for $SrCl_2$: La^{2+} at approximately 6 °K for $\vec{H} \parallel \langle 110 \rangle$ and $\vec{H} \parallel \langle 111 \rangle$. The first derivative of absorption is shown versus magnetic field.

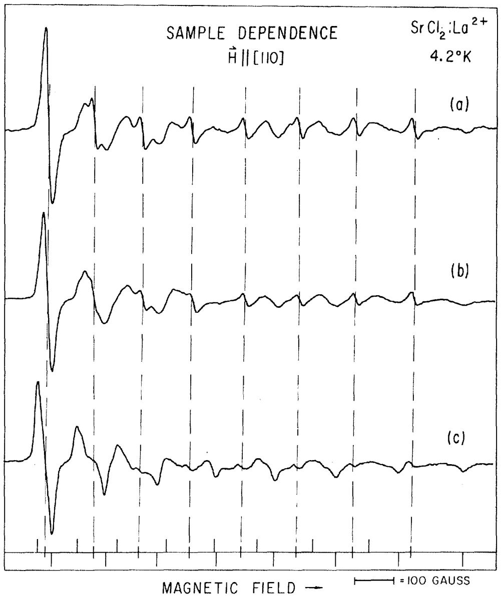

FIG. 8. EPR spectrum observed ($\nu = 8.9$ GHz) at 4.2 °K and at a $\langle 110 \rangle$ orientation of the applied magnetic field for $SrCl_2$: La samples reduced in Sr vapor for (a) 30 min (b) 15 min, and (c) 5 min. The first derivative of absorption is shown versus magnetic field. The extrema of the components of the anisotropic pattern are located by vertical bars on the horizontal scale below the traces. The isotropic lines are located by the dashed vertical lines.

The condition for averaging by relaxation is that the relaxation rate for processes of the type indicated in Fig. 1 by wavy arrows must satisfy the following relation[22–25]:

$$\tau^{-1} \gg 2\pi \Delta\nu \ . \qquad (13)$$

For a system exhibiting a dynamic Jahn-Teller effect for an orbital doublet, random strains cause the characteristic line shape discussed in Sec. II and illustrated in Fig. 2. This composite line is the result of a large number of overlapping lines due to transitions within the strain-split ^2E_g ground vibronic states. In first order, these transitions occur in pairs symmetrically placed about the center of the envelope. Thus, if $\tau^{-1} \neq 0$ for these vibronic relaxation processes, then Eq. (13) is satisfied for those transitions occurring sufficiently close to the center of the envelope and averaging of these transitions will occur as illustrated in Fig. 9. (For a more detailed discussion of the line shapes encountered due to averaging by rapid relaxation, see Watkins and Ham.[25])

The extrema of each component of the anisotropic pattern vary as a function of the orientation of the applied field according to Eqs. (10) and (11) and therefore produce a change in that portion of each component of the anisotropic pattern satisfying Eq.

(13). The intensity of each line in the isotropic pattern will then vary as a function of the applied magnetic field orientation, i.e., as the field approaches a ⟨111⟩ orientation, that portion of each component of the anisotropic pattern satisfying Eq. (13) increases producing a corresponding increase in the intensity of the lines in the isotropic pattern. This variation was observed in Figs. 5 and 6.

For a general orientation of the applied field, the difference in field position between the extrema for each component of the anisotropic pattern increases with magnetic field, see Fig. 4 (the exceptional orientation being the ⟨111⟩). As a result, that portion of each component of the anisotropic pattern satisfying Eq. (13) decreases with increasing magnetic field producing a corresponding decrease in the intensity of the lines in the isotropic pattern. This variation is seen in Figs. 5 and 6 but is most striking in Fig. 7.

The components of the isotropic pattern were observed to increase in apparent intensity with increasing temperature. At the same time the peaks in the anisotropic pattern were observed to broaden with increasing temperature. This broadening of the peaks of the components of the anisotropic pattern indicated that the individual lines composing the components were broadening as the temperature increased. This broadening is a result of the rapid vibronic ($\Delta m_S = 0$) relaxation between the strain-split levels.

Ham[17] has discussed three relaxation processes (a direct, a Raman, and an Orbach process) which could produce averaging by relaxation. The relaxation rates for these processes are characterized by different temperature dependences. Measurements of the apparent intensities of the components of the isotropic pattern indicated an approximately linear temperature dependence between 1.2 and 4.2 °K (see Figs. 5 and 6). This implies that the relaxation rate τ^{-1} increases approximately linearly with temperature and in this way increases that portion of each of the components of the anisotropic pattern which average. This linear variation of the relaxation rate is characteristic of a direct process. At temperatures near 6 °K, the anisotropic components of the La^{2+} spectrum are broadened beyond detection. This implies that at this temperature, the relaxation rate τ^{-1} is on the order of the difference in frequency between the extrema for the high-field component of the pattern for $\vec{H}$ parallel to a ⟨100⟩ direction. Above 10 °K, the apparent intensity of each line in the isotropic pattern was observed to be independent of magnetic field orientation and each line was observed to have the same linewidth implying that the averaging of the anisotropic components of the spectrum was complete. This rapid change in τ^{-1} between approximately 6 and 10 °K probably implies the onset of the other relaxation processes.

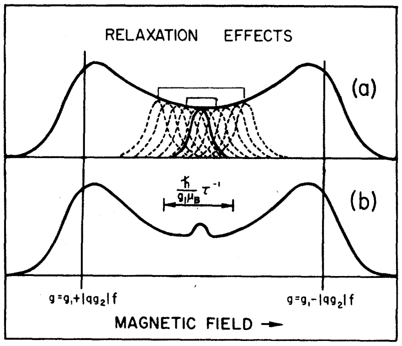

FIG. 9. EPR line shape in first order without (a) and with (b) rapid vibronic relaxation ($\Delta m_S = 0$) between the strain-split states. The absorption is shown versus magnetic field with the extrema of the envelope located by the vertical lines. The relaxation rate for the processes causing averaging is denoted by τ^{-1}. The effective g values for the extrema contain the function f defined in Eq. (8).

For the direct process, the expression for the relaxation rate in the long-wavelength limit[16,17] is

$$\tau^{-1} = \frac{3\delta^3(qV_s)^2}{20\pi\hbar^4\rho s_T^5}\left[1 + \frac{2}{3}\left(\frac{s_T}{s_L}\right)^5\right]\coth\frac{\delta}{2kT}, \tag{14}$$

where δ is the strain splitting (see Fig. 1), qV_s is the strain coupling parameter, ρ is the crystal density, and s_T and s_L are, respectively, the transverse and longitudinal speed of sound. The dependence of the relaxation rate τ^{-1} on δ offers an obvious explanation for the observed dependence of the intensity of the isotropic pattern relative to the anisotropic pattern (see Fig. 8) on the time each sample was reduced by Sr vapor. The longer the samples were subjected to the vapor, the more severely the crystals were strained internally. The direct process alone is characterized by a relaxation rate dependent on δ. This conclusion is consistent with later observations that the isotropic pattern in samples reduced using γ radiation was comparable to that seen in samples reduced with Sr vapor for times on the order of 5 min. In addition, EPR was not observed for samples reduced in Sr vapor for times longer than about 40 min and these samples easily fractured indicating very large internal strains.

C. Other Features

With the applied magnetic field oriented in a ⟨111⟩ direction, seven additional lines were observed at 1.2 °K and at high gain. Each of these lines occurred approximately halfway between one of the seven pairs of adjacent components of the anisotropic pattern. Due to the angular variation of the anisotropic pattern, these lines were observed only near a ⟨111⟩ orientation. The position, low intensity, and number of these lines are characteristic of

$\Delta m_S = \pm 1$, $\Delta m_I = \pm 1$ transitions. An analysis of these these transitions is in progress and the results will be reported in a forthcoming paper.

Between 11 and 16 °K, a single line near $g = 2$ was observed to coexist with the isotropic pattern discussed in Sec. IV B, Fig. 10. This line increased in apparent intensity as the temperature increased, and near 16 °K it began to dominate the spectrum. At about 20 °K, this line began to broaden but was observed to approximately 40 °K. Above this temperature, EPR was not observed. It is interesting to note that a similar line occurs for Sc^{2+} complexes.[9,10] This line was observed in samples reduced using γ radiation and Sr vapor and will be studied in detail in later investigations.

V. IMPLICATIONS OF MODERATE VIBRONIC-COUPLING MODEL

In Sec. II B, the coupling parameters used in the effective Hamiltonian (i.e., $g_1 \mu_B$, $\frac{1}{2} q g_2 \mu_B$, A_1, $\frac{1}{2} q A_2$, and $q V_s$) included Ham's reduction factor[16,17] q explicitly. Hence the parameters g_1, g_2, A_1, A_2, and V_s would be characteristic of the ^2E_g orbital state with zero vibronic coupling and could then be calculated using crystal field theory. To first order in λ/Δ, crystal field theory predicts that these parameters are given by the following expressions:

$$g_1 = 2.0023 - 4\lambda/\Delta\ , \tag{15}$$

$$g_2 = -4\lambda/\Delta\ , \tag{16}$$

$$A_1 = -2\mu_B \langle r^{-3}\rangle \frac{\mu}{I}\left(\kappa + 4\frac{\lambda}{\Delta}\right), \tag{17}$$

$$A_2 = -2\mu_B \langle r^{-3}\rangle \frac{\mu}{I}\left(\frac{4}{7} + \frac{34}{7}\frac{\lambda}{\Delta}\right). \tag{18}$$

The parameters λ, Δ, μ_B, $\langle r^{-3}\rangle$, μ, I, and κ are, respectively, the Russell-Saunders spin-orbit coupling parameter, the cubic crystal field splitting, the Bohr magneton, the dipole moment and spin of the ^{139}La nucleus, and the Fermi contact hyperfine parameter. Using those values for the parameters g_1, qg_2, A_1, and qA_2 listed in Table I and Eqs. (15)—(18), it is possible to obtain estimates for some of the more basic parameters (i.e., Δ, q, κ, δ, and τ^{-1}) associated with the model for $SrCl_2:La^{2+}$ illustrated in Fig. 1.

The ratio λ/Δ was estimated using the parameter g_1 listed in Table I and Eq. (15). This ratio, approximately 0.03, together with the spin-orbit parameter λ for the La^{2+} free ion, approximately 650 cm^{-1} as predicted from the free-ion fine-structure splitting for the ground ^2D term, implied that the cubic crystal field splitting $10Dq$ or Δ in Fig. 1 was on the order of 21 000 cm^{-1}. The actual crystal field splitting is expected to be somewhat less due to the reduction of λ from its free-ion value, but 20 000 cm^{-1} should be a reasonable order-of-magnitude estimate.

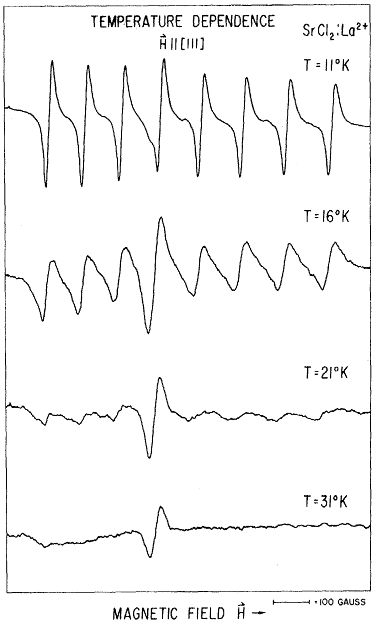

FIG. 10. Temperature dependence of the EPR spectrum observed ($\nu = 9.3$ GHz) for $SrCl_2:La^{2+}$ samples at a $\langle 111\rangle$ orientation of the applied magnetic field at $T = 11$ °K, $T = 16$ °K, $T = 21$ °K, and $T = 31$ °K. The first derivative of absorption is shown versus magnetic field.

From Eq. (16), the value of the parameters qg_2 in Table I and λ/Δ determined above, a value for q on the order of 0.57 ± 0.02 is implied. Together with the ratio A_1/qA_2, approximately 6.36, Eqs. (17) and (18), and λ/Δ determined above, this value for q implies that the Fermi contact hyperfine parameter is on the order of 2.5. This is ample evidence for appreciable configuration interaction or core polarization which is to be expected for ions with an incomplete $5d$ shell.[26]

The deviation of the reduction factor observed from the value $\frac{1}{2}$ implies that the Jahn-Teller energy E_{JT} is on the order of $\hbar\omega$, where $\hbar\omega$ corresponds to the average energy of the optical mode of vibration for $SrCl_2$. Typical values of $\hbar\omega$ for fluorite structures are on the order of 300 cm^{-1}, thus $E_{JT} \approx 300$ cm^{-1}. In addition the ratio $E_{JT}/\hbar\omega \simeq 1.0$ implies that the first-excited vibronic state is located some 140 cm^{-1} above the ground state. Thus, the ground vibronic doublet should behave like an isolated ^2E_g state, a conclusion consistent with our observations.

In Sec. IV B, the anisotropic pattern was observed to broaden beyond detection in the temperature range 4.2–10 °K. This implied that the relaxation rate for the direct process τ^{-1} was on the order of 1.5×10^9 Hz, the approximate difference in frequency between the extrema of the high-field component of the anisotropic pattern for $\vec{H} \parallel \langle 100\rangle$. Using the relation between the Jahn-Teller energy and the strain-coupling parameter V_s derived by Ham[16, 17] to obtain $qV_s \approx 1.2 \times 10^4$ cm^{-1}, the approximate speeds of sound $s_L \approx 6\times 10^5$ cm/sec and $s_T \approx 3\times 10^5$ cm/sec for $SrCl_2$, the approximate relaxation rate $\tau^{-1} \approx 2\times 10^9$ Hz at 7 °K, and Eq. (14), one predicts a typical strain splitting δ on the order of 1 cm^{-1}. Since most crystals have internal strains on the order of 10^{-4}–10^{-5}, such a strain splitting is not surprising. Thus with a strain splitting on the order of 1 cm^{-1}, the relaxation rate predicted for the direct process is consistent with our observations. Indeed at temperatures on the order of 1.2 °K where the isotropic pattern begins to emerge, the direct process is expected to be dominant.

VI. SUMMARY AND CONCLUSIONS

The EPR spectrum for $SrCl_2$: La^{2+} has been observed as a function of temperature between 1.2 and 40 °K and as a function of sample treatment. In all samples at 1.2 °K, the spectrum was observed to consist of three distinct patterns: (a) an intense eight-component anisotropic pattern, (b) a weak eight-line isotropic pattern, and (c) a very weak seven-line pattern. The intensity of the eight-line isotropic pattern relative to the eight-component anisotropic pattern was observed to vary with the time of reduction with Sr vapor. Between 1.2 °K and 4.2 °K, the individual transitions composing each envelope in the anisotropic pattern were observed to broaden with increasing temperature while the intensity of each of the eight isotropic lines increased approximately linearly with temperature. Near 6 °K, the components of the anisotropic pattern were broadened beyond detection. Between 6 and approximately 10 °K only the eight-line isotropic pattern was observed. Between approximately 10 and 30 °K, the lines in the eight-line isotropic pattern were observed to broaden while a single line near $g = 2$ emerged. This single isotropic line was observed between approximately 15 and 40 °K, and at temperature greater than 40 °K, no EPR was seen.

The line shapes of the individual components of the anisotropic pattern seen at 1.2 °K were characteristic of large random internal strains. The extrema of these components were fitted within experimental accuracy using second-order solutions of Ham's effective Hamiltonian for an isolated ^2E_g state[16, 17] in cubic symmetry. The parameters resulting from this fit are listed in Table I. In addition to large random internal strains, the $SrCl_2$: La^{2+} crystals showed some evidence of mosaic structure. The very weak seven-line pattern is believed due to $\Delta m_I = \pm 1$ forbidden transitions and will be discussed in a forthcoming paper.

From the variation of the apparent intensity of the components in the eight-line isotropic pattern with temperature, sample treatment, and applied field orientation, we conclude that this pattern is due to averaging of a portion of the anisotropic pattern caused by rapid direct relaxation between the random strain-split components of the ^2E_g ground vibronic state. Similar patterns reported for other complexes[6–10, 18, 19] exhibiting a dynamic Jahn-Teller effect have been interpreted as due to thermal population of nearby excited "tunneling" singlet, but none of the above characteristics of this pattern are consistent with this "tunneling" singlet hypothesis.

In conclusion, with the possible exception of the isotropic line near $g = 2$, all features of the EPR spectrum for $SrCl_2$: La^{2+} are understood based on the assumption that the ground state for the paramagnetic complex is a ^2E_g state and no other state is close in energy. The reduction of certain parameters in the effective Hamiltonian from values predicted for a ^2E_g orbital state of La^{2+} using crystal field theory implies that the ground state is a vibronic state and the predictions of Ham's moderate vibronic-coupling model[16, 17] are consistent with our observations.

ACKNOWLEDGMENTS

We would like to acknowledge the contributions of Dr. B. Dischler in the early phases of this work and for his excellent comments on the manuscript. We acknowledge with thanks the hospitality of Dr. P. P. Mahendroo and the assistance of H. B. Utley in utilizing the cryotip refrigerator at Texas Christian University for some of the 10–30 °K observations. In addition, we would like to thank Dr. R. J. Shalek for his generosity in permitting our use of the ^{137}Cs facility at the Research and Tumor Institute, M. D. Anderson Hospital, University of Texas, for sample irradiation. The able technical assistance of E. G. Clardy in several phases of the work is also gratefully acknowledged. We are further indebted to Dr. L. L. Chase for providing us with information concerning his work with Eu^{2+} prior to publication and to Dr. F. S. Ham for enlightening discussions of the manuscript.

APPENDIX A: SOLUTION FOR EFFECTIVE HAMILTONIAN OF EQ. (2)

Consider the effective Hamiltonian of Eq. (2) partitioned into $\mathcal{H}_0$ and $\mathcal{H}_1$ given by

$$\mathcal{H}_0 = q\,V_s(e_\theta \mathcal{E}_\theta + e_\epsilon \mathcal{E}_\epsilon) \ , \tag{A1}$$

$$\mathcal{H}_1 = g_1\,\mu_B\,\vec{\mathrm{H}}\cdot\vec{\mathrm{S}}\,\mathcal{A}_1 + \tfrac{1}{2} q g_2\,\mu_B[(3H_z S_z - \vec{\mathrm{H}}\cdot\vec{\mathrm{S}})\,\mathcal{E}_\theta + \sqrt{3}\,(H_x S_x - H_y S_y)\,\mathcal{E}_\epsilon] \ . \tag{A2}$$

Assuming that the strain interaction $\mathcal{H}_0$ determines the admixture of the $|\theta\rangle$ and $|\epsilon\rangle$ vibronic states one obtains the two eigenfunctions

$$|+\rangle = \sin\tfrac{1}{2}\varphi\ |\theta\rangle + \cos\tfrac{1}{2}\varphi\ |\epsilon\rangle \ ,$$

$$|-\rangle = \cos\tfrac{1}{2}\varphi\,|\theta\rangle - \sin\tfrac{1}{2}\varphi\,|\epsilon\rangle \quad . \tag{A3}$$

In this high-strain limit, the coupling between the $|+\rangle$ and $|-\rangle$ states may be neglected and these vibronic states may be treated independently. The operator for the Zeeman interaction $\mathcal{H}_1$ for the $|+\rangle$ state is given by Eq. (A4) and $\mathcal{H}_1$ for the $|-\rangle$ state is given by Eq. (A5):

$$\mathcal{H}_1^+ = \langle +\,|\mathcal{H}_1|\,+\rangle = g_1\mu_B\vec{\mathrm{H}}\cdot\vec{\mathrm{S}} + \tfrac{1}{2}qg_2\mu_B[(3H_zS_z - \vec{\mathrm{H}}\cdot\vec{\mathrm{S}})\cos\varphi + \sqrt{3}\,(H_xS_x - H_yS_y)\sin\varphi] \;, \tag{A4}$$

$$\mathcal{H}_1^- = \langle -\,|\mathcal{H}_1|\,-\rangle = g_1\mu_B\vec{\mathrm{H}}\cdot\vec{\mathrm{S}} - \tfrac{1}{2}qg_2\mu_B[(3H_zS_z - \vec{\mathrm{H}}\cdot\vec{\mathrm{S}})\cos\varphi + \sqrt{3}\,(H_xS_x - H_yS_y)\sin\varphi] \;, \tag{A5}$$

The Zeeman interactions in Eqs. (A4) and (A5) may be represented in terms of the coupling tensors $\overleftrightarrow{\mathrm{g}}^+$ and $\overleftrightarrow{\mathrm{g}}^-$ in the following manner:

$$\mathcal{H}_1^+ = \mu_B\vec{\mathrm{H}}\cdot\overleftrightarrow{\mathrm{g}}^+\cdot\vec{\mathrm{S}} \;, \tag{A6}$$

$$\mathcal{H}_1^- = \mu_B\vec{\mathrm{H}}\cdot\overleftrightarrow{\mathrm{g}}^-\cdot\vec{\mathrm{S}} \;, \tag{A7}$$

where the components of the coupling tensors $\overleftrightarrow{\mathrm{g}}^+$ and $\overleftrightarrow{\mathrm{g}}^-$ are given by

$$\begin{aligned} g_{xx}^{\pm} &= g_1 \pm \tfrac{1}{2}qg_2(-\cos\varphi + \sqrt{3}\sin\varphi) \;, & g_{xy}^{\pm} &= g_{yx}^{\pm} = 0 \;, \\ g_{yy}^{\pm} &= g_1 \pm \tfrac{1}{2}qg_2(-\cos\varphi - \sqrt{3}\sin\varphi) \;, & g_{yz}^{\pm} &= g_{zy}^{\pm} = 0 \;, \\ g_{zz}^{\pm} &= g_1 \pm qg_2\cos\varphi \;, & g_{zx}^{\pm} &= g_{xz}^{\pm} = 0 \;. \end{aligned} \tag{A8}$$

Choosing the axis of quantization for $\vec{\mathrm{S}}$ in Eq. (A6) parallel to the vector $\vec{\mathrm{H}}\cdot\overleftrightarrow{\mathrm{g}}^+$ and in Eq. (A7) parallel to $\vec{\mathrm{H}}\cdot\overleftrightarrow{\mathrm{g}}^-$ one obtains the following energies:

$$\begin{aligned} E_{m_S}^+ &= qV_s(e_\theta^2 + e_\epsilon^2)^{1/2} + \mu_B\,|\vec{\mathrm{H}}\cdot\overleftrightarrow{\mathrm{g}}^+|\,m_S \;, \\ E_{m_S}^- &= -qV_s(e_\theta^2 + e_\epsilon^2)^{1/2} + \mu_B\,|\vec{\mathrm{H}}\cdot\overleftrightarrow{\mathrm{g}}^-|\,m_S \;. \end{aligned} \tag{A9}$$

The scalars $|\vec{\mathrm{H}}\cdot\overleftrightarrow{\mathrm{g}}^{\pm}|$ are given by

$$|\vec{\mathrm{H}}\cdot\overleftrightarrow{\mathrm{g}}^{\pm}| = H(l^2g_{xx}^{\pm 2} + m^2g_{yy}^{\pm 2} + n^2g_{zz}^{\pm 2})^{1/2} \;, \tag{A10}$$

when $g_{ii}^{\pm}$ are given by Eq. (A8), H is the magnitude of the magnetic field and l, m, and n are the direction cosines of the applied magnetic field with respect to the cubic axes. Substitution of Eq. (A8) into Eq. (A10), simplifying, and then substituting into Eq. (A9) yields Eq. (3).

APPENDIX B: SOLUTION FOR EFFECTIVE HAMILTONIAN OF EQ. (9)

Consider the effective Hamiltonian of Eq. (9) partitioned into $\mathcal{H}_0$ and $\mathcal{H}_1$ given by

$$\mathcal{H}_0 = gV_s(e_\theta\mathcal{E}_\theta + e_\epsilon\mathcal{E}_\epsilon) \;, \tag{B1}$$

$$\begin{aligned} \mathcal{H}_1 = g_1\mu_B\beta\vec{\mathrm{H}}\cdot\vec{\mathrm{S}}\,\mathcal{A}_1 &+ \tfrac{1}{2}qg_2\mu_B[(3H_zS_z - \vec{\mathrm{H}}\cdot\vec{\mathrm{S}})\mathcal{E}_\theta \\ &+ \sqrt{3}\,(H_xS_x - H_yS_y)\mathcal{E}_\epsilon] + A_1\vec{\mathrm{I}}\cdot\vec{\mathrm{S}}\,\mathcal{A}_1 \\ &+ \tfrac{1}{2}qA_2[(3I_zS_z - \vec{\mathrm{I}}\cdot\vec{\mathrm{S}})\grave{o}_\theta + \sqrt{3}\,(I_xS_x - I_yS_y)\mathcal{E}_\epsilon] \;. \end{aligned} \tag{B2}$$

Assuming that the admixture of the vibronic states $|\theta\rangle$ and $|\epsilon\rangle$ are determined by $\mathcal{H}_0$ one obtains the eigenfunctions for the $|+\rangle$ and $|-\rangle$ states given in Eq. (A3). The coupling between the $|+\rangle$ and $|-\rangle$ states may be neglected in this high-strain limit and these states may be treated independently. The Hamiltonian $\mathcal{H}_1$ for the $|+\rangle$ is given in Eq. (B3) and for the $|-\rangle$ state in Eq. (B4):

$$\begin{aligned} \mathcal{H}_1^+ = g_1\mu_B\,\vec{\mathrm{H}}\cdot\vec{\mathrm{S}} &+ \tfrac{1}{2}qg_2\mu_B\,[(3H_zS_z - \vec{\mathrm{H}}\cdot\vec{\mathrm{S}})\cos\varphi \\ &+ \sqrt{3}\,(H_xS_x - H_yS_y)\sin\varphi] + A_1\vec{\mathrm{I}}\cdot\vec{\mathrm{S}} \\ &+ \tfrac{1}{2}qA_2[(3I_zS_z - \vec{\mathrm{I}}\cdot\vec{\mathrm{S}})\cos\varphi + \sqrt{3}\,(I_xS_x - I_yS_y)\sin\varphi] \;, \end{aligned} \tag{B3}$$

$$\begin{aligned} \mathcal{H}_1^- = g_1\mu_B\vec{\mathrm{H}}\cdot\vec{\mathrm{S}} &- \tfrac{1}{2}qg_2\mu_B[(3H_zS_z - \vec{\mathrm{H}}\cdot\vec{\mathrm{S}})\cos\varphi \\ &+ \sqrt{3}\,(H_xS_x - H_yS_y)\sin\varphi] + A_1\vec{\mathrm{I}}\cdot\vec{\mathrm{S}} \\ &- \tfrac{1}{2}qA_2[(3I_zS_z - \vec{\mathrm{I}}\cdot\vec{\mathrm{S}})\cos\varphi + \sqrt{3}\,(I_xS_x - I_yS_y)\sin\varphi] \;. \end{aligned} \tag{B4}$$

Computing the relations between the components of the vectors $\vec{\mathrm{S}}$, $\vec{\mathrm{H}}$, and $\vec{\mathrm{I}}$ with respect to the cubic axis system (x, y, z) and the components of the same vectors with respect to a new coordinate system (x', y', z') where the z' axis is chosen parallel to the magnetic field vector, the x' axis is chosen perpendicular to z' axis in the xy plane, and the y' axis is chosen to complete a right-handed orthogonal triad with x' and z', one obtains the following linear transformation:

$$\begin{pmatrix} x \\ y \\ z \end{pmatrix} = \begin{pmatrix} m/\gamma & ln/\gamma & l \\ -l/\gamma & mn/\gamma & m \\ 0 & -\gamma & n \end{pmatrix} \begin{pmatrix} x' \\ y' \\ z' \end{pmatrix} . \tag{B5}$$

Substituting for the components of $\vec{\mathrm{S}}$, $\vec{\mathrm{H}}$, and $\vec{\mathrm{I}}$ with respect to the (x, y, z) coordinate system in Eqs. (B3) and (B4) the correct combinations of the components of $\vec{\mathrm{S}}$, $\vec{\mathrm{H}}$, and $\vec{\mathrm{I}}$ with respect to the (x', y', z') coordinate system determined using Eq. (B5) and simplifying yields the following:

$$\begin{aligned} \mathcal{H}_1^{\pm} = (g_1 \pm \tfrac{1}{2}qg_2f_1)\mu_BH_{z'}S_{z'} &\pm qg_2\mu_BH_{z'}(f_5\,{}_{+'} + f_5^*S_{-'}) \\ &+ (A_1 \pm \tfrac{1}{2}qA_2f_1)\mathrm{I}_{z'}S_{z'} \pm qA_2[f_5(I_{+'}S_{z'} + I_{z'}S_{+'}) \\ &+ f_5^*(I_{-'}S_{z'} + S_{-'}I_{z'})] + \tfrac{1}{2}(A_1 \mp \tfrac{1}{4}qA_2f_1)(I_{+'}S_{-'} + I_{-'}S_{+'}) \\ &\pm qA_2(f_6I_{+'}S_{+'} + f_6^*I_{-'}S_{-'}) \;. \end{aligned} \tag{B6}$$

The function f_1 was defined in Eq. (11) and the primed raising and lowering operators are defined by

$$I_{+'} = I_{x'} + i\, I_{y'}\,, \quad S_{+'} = S_{x'} + i S_{y'}\,,$$
$$I_{-'} = I_{x'} - iI_{y'}, \quad S_{-'} = S_{x'} - i S_{y'}\,, \tag{B7}$$

with the functions f_4 and f_5 defined by

$$f_5 = \frac{\sqrt{3}}{2}\left(\frac{lm}{\gamma} + \frac{(l^2 - m^2)n}{2i\gamma}\right)\sin\varphi - \frac{3\gamma n}{4i}\cos\varphi\,, \tag{B8}$$

$$f_6 = \frac{\sqrt{3}}{2}\left(\frac{lmn}{i\gamma^2} - \frac{(l^2 - m^2)(1 + n^2)}{4\gamma^2}\right)\sin\varphi - \frac{3\gamma^2}{8}\cos\varphi\,,$$

with $\gamma^2 = l^2 + m^2$. Substituting the standard spin operators in Eq. (B6) assuming both $\vec{S}$ and $\vec{I}$ are quantized along the z' axis, computing the energies for the states to second order and computing the EPR transition frequencies using the selection rules $\Delta m_S = \pm 1$, $\Delta m_I = 0$, one obtains

$$h\nu_{\pm} = \left(g_1 \pm \tfrac{1}{2} q g_2 f_1 + \frac{(q g_2)^2}{g_1} f_3\right)\mu_B H + \left(\frac{(A_1 \mp \frac{1}{4} q A_2 f_1)^2}{2 g_1 \mu_B H} + \frac{(qA_2)^2 f_4}{g_1 \mu_B H}\right)[I(I+1) - m_I^2] + \left[A_1 \pm \tfrac{1}{2} q A_2 f_1 + \frac{(qA_2)^2}{A_1} f_3 + 2\left(\frac{q g_2}{g_1}\right) q A_2 f_3\right] m_I + \frac{(qA_2)^2}{g_1 \mu_B H} f_3 m_I^2\,. \tag{B9}$$

The functions f_1, f_3, and f_4 were defined in Eq. (11). Solving for the magnetic field positions of the transitions one obtains Eq. (10).

---

*Work supported by the National Aeronautics and Space Administration and the National Science Foundation.

†Formerly LTV Research Center.

[1] H. A. Jahn and E. Teller, Proc. Roy. Soc. (London) A161, 220 (1937).

[2] B. Bleaney and K. D. Bowers, Proc. Phys. Soc. (London) A65, 667 (1952).

[3] B. Bleaney and D. J. E. Ingram, Proc. Phys. Soc. (London) A63, 408 (1950).

[4] A. Abragam and M. H. L. Pryce, Proc. Phys. Soc. (London) A63, 409 (1950).

[5] M. D. Sturge, in *Solid State Physics*, edited by F. Seitz, D. Turnbull, and H. Ehrenreich (Academic, New York, 1967), Vol. 20, p. 91.

[6] R. E. Coffman, Phys. Letters 19, 475 (1965).

[7] R. E. Coffman, Phys. Letters 21, 381 (1966).

[8] R. E. Coffman, J. Chem. Phys. 48, 609 (1968).

[9] U. T. Höchli and T. L. Estle, Phys. Rev. Letters 18, 128 (1967).

[10] U. T. Höchli, Phys. Rev. 162, 262 (1967).

[11] R. E. Coffman, D. L. Lyle, and D. R. Mattison, J. Phys. Chem. 72, 1392 (1968).

[12] I. B. Bersuker, Zh. Eksperim. i Teor. Fiz. 43, 1315 (1962) [Sov. Phys. JETP 16, 933 (1963)].

[13] I. B. Bersuker, Zh. Eksperim. i Teor. Fiz. 44, 1239 (1963) [Sov. Phys. JETP 17, 836 (1963)].

[14] I. B. Bersuker and B. G. Vekhter, Fiz. Tverd. Tela 5, 2432 (1963) [Sov. Phys. Solid State 5, 1772 (1964)].

[15] M. C. M. O'Brien, Proc. Roy. Soc. (London) A281, 323 (1964).

[16] F. S. Ham, Phys. Rev. 166, 307 (1968).

[17] F. S. Ham, in *Electron Paramagnetic Resonance*, edited by S. Geschwind (Plenum, New York, to be published).

[18] L. L. Chase, Phys. Rev. Letters 23, 275 (1969).

[19] L. L. Chase, Phys. Rev. B 2, 2308 (1970).

[20] L. A. Boatner, B. Dischler, J. R. Herrington, and T. L. Estle, Bull. Am. Phys. Soc. 14, 355 (1969).

[21] J. R. Herrington, T. L. Estle, L. A. Boatner, and B. Dischler, Phys. Rev. Letters 24, 984 (1970).

[22] H. S. Gutowsky, D. W. McCall, and C. P. Slichter, J. Chem. Phys. 21, 279 (1953).

[23] H. M. McConnell, J. Chem. Phys. 28, 430 (1958).

[24] A. Abragam, *The Principles of Nuclear Magnetism* (Oxford U. P., Oxford, England, 1961), Chap. 10.

[25] G. D. Watkins and F. S. Ham, Phys. Rev. B 1, 4071 (1970).

[26] A. Abragam and B. Bleaney, *Electron Paramagnetic Resonance of Transition Ions* (Oxford U. P., Oxford, England, 1970), Sec. 17.6.